OPTICAL CALIBRATION OF THE M4 PROTOTYPE TOWARD THE FINAL UNIT

Runa Briguglio[1a], Giorgio Pariani[2], Marco Xompero[1], Armando Riccardi[1], Mario Andrighettoni[3], Roberto Biasi[3], Matteo Tintori[4], and Daniele Gallieni[4]

[1] INAF, Arcetri Observatory, p. E. Fermi 5, 50125 Firenze, Italy
[2] INAF, Merate Observatory, Via E. Bianchi 46, 23807 Merate (Lc) Italy
[3] Microgate, via Stradivari 4, 39100 Bolzano, Italy
[4] ADS-International, via Roma 87, 23868 Valmadrera (Lc) Italy

Abstract. The M4DP is the demonstration prototype of the E-ELT adaptive mirror M4. The optical calibration and test of the M4DP, held in INAF laboratories during February and March 2015, has been a lesson learned for the forthcoming optical verification of the 5000 actuators, 6 segments final unit. The test procedure was tailored to fit the peculiarities of such 2 segments, 222 actuators prototype. Key elements are the simultaneous segments control and the measurement and correction of the rigid modes over the segmented pupil; convection noise affecting the phasing was also investigated. In this paper we will report the results of the optical test and the specific solutions implemented for the phasing control and performance verification.

1 Introduction

The on-sky capabilities of adaptive secondary mirrors (ASM) has been shown since the first test on the MMT[1] and the following ASM development for LBT[3] demonstrated its effectiveness for high contrast AO systems. Through the years, many secondaries have been commissioned and offered to the scientific community; in the next future more complex systems will be manufactured and integrated, such as the M4[2] for the E-ELT.
Differently from previous cases[3][4], the procedure for the optical calibration of such DM will include new features, for instance the simultaneous segments control and the correction of global modes for phasing. In the mainframe of the M4 project, AdOptica built up a demonstration prototype composed by two shells with 222 actuators on a monolithic reference plate. The system served as a bench for testing and optimizing the electro-mechanical solutions proposed for the M4; the tests were concluded with the optical verification: a first run[5] was carried out in 2010 and a second run, after a major refurbishment of the system, presented here.

Within the scope of the optical testing of the M4DP, we implemented a calibration procedure fitting the new features of both the DP and the M4; the measurement campaign provided a demonstration of the proposed procedure and a lesson learned to improve it for the final unit, which should be ready for optical testing in 2021.

[a] runa@arcetri.astro.it

2 The M4 Demostration Prototype on the test bench

After the successful completion of the electro-mechanical tests, the M4DP was installed on the optical bench inside an ISO 7 clean room at INAF in order to start the optical verification. The M4DP was mounted facing down in a Ritchey-Common Test (RCT) configuration. The f/5 cavity from the interferometer (4D Technology PhaseCam 4020 vibration insensitive system) was closed by a high quality 500 mm diameter spherical mirror (SM). The M4DP folded the cavity at a RCT angle of 64° on the chief ray. Two auxiliary folding mirrors were used to center the pupil on the interferometer and align the cavity. In Fig.1 the optical bench is shown.

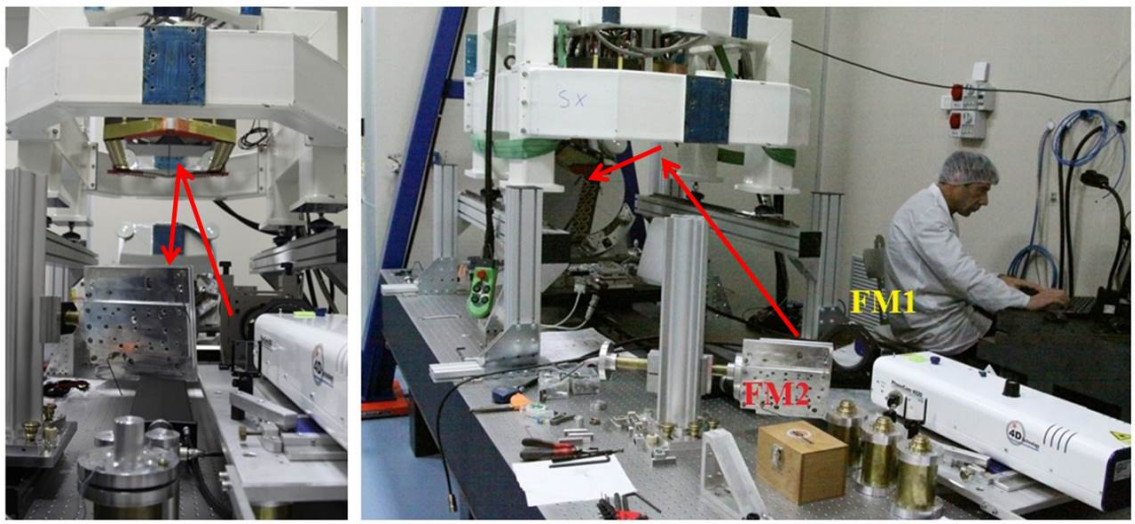

Fig. 1. The M4DP system installed on the bench at INAF-Merate, showing the optical setup and the propagation of the laser beam.

Because of the beam oblique incidence on the M4DP, both the spatial sampling and the wedge factor were varying across the interferometer image. The geometrical transformation between pupil coordinates (on the spherical mirror) and surface coordinates (on the M4DP) consists in i) the rotation of the image on the pupil center and ii) a morphing effect caused by the RCT angle. The image rotation is caused by the skew optical layout of the RCT system, since the interferometer optical axis and the sphere axis passing for the pupil center are not coplanar. The morphing effect is due to the incidence angle of the beam on the M4DP, and to its local variations on the M4DP surface itself.

Along with the non-constant incidence angle on the M4DP surface, the wedge factor varies accordingly. A surface error Δs on the M4DP surface (with coordinates x_s, y_s) turns into a wavefront error Δz seen by the interferometer

$$\Delta z = 2 \cdot 2\Delta s(x_s, y_s) \cos \xi(x_s, y_s)$$

where ξ is the local incidence angle. A 2x factor is due to reflection on the mirror surface, and the further 2x factor takes into account the double-pass over the M4DP. Accordingly, the M4DP surface can be retrieved from

$$SF_{DP} = WFE_{RCT}/(4cos\xi)$$

Starting from the literature[6], a routine was written to accomplish the morphing and the wavefront-to-surface transformation. Geometric parameters (RCT angle, SM diameter, and M4DP to SM

distance), which were requested to proper initialize the transformation algorithm, were measured with a laser tracker and best-fitted using the actuator positions on the image as markers.

In the optical test we considered the RCT cavity WFE directly measured by the interferometer and retrieve from that the M4DP surface error by means of the transformation algorithm after alignment compensation. The telescope WFE was approximated as

$$WFE_{EELT} = 2SF_{DP}$$

considering that on the EELT a nearly collimated beam will be projected onto the M4 surface. Accordingly, the flattening procedure was run considering both the modal IF and the mirror shape as from the RCT measurement. We verified by simulation that the minimization algorithm of the flattening procedure yields the same results when comparing the RCT bask-transformed flats with that obtained with RCT back-transformed IF and reference image.

3 Optical calibration procedure tailored on the M4DP

The optical calibration procedure developed for previous adaptive mirrors such as the LBT and the VLT was modified to match the M4DP. In this section we will describe the specific implementation, addressing in particular the system segmentation, the control of actuators below the lateral membranes and the test of large amplitude Zernike commands. The procedure results will be presented and discussed in Sec.4.

3.1 Startup of a segmented unit

The mirror is commanded through a 222x222 command matrix V whose vectors are the stiffness eigenmodes of the system (intended as an electro-mechanical ensemble). V is computed by singular value decomposition of the *feed-forward* matrix FF: more details about FF and system eigenmodes may be found in [7]. Given the system segmentation into two electrically decoupled units, both FF and V are blocks diagonal, in the form (e.g.)

$$V = \begin{pmatrix} V_0 & 0 \\ 0 & V_1 \end{pmatrix}$$

where V_0 and V_1 are the command matrices of the single subsystems (mirror segments); the same applies for the FF matrix. The not-diagonal elements have been replaced with zeroes to reject measurement noise. The V matrix is shown in Fig.2.
Such scheme is appealing for communication as in the final unit: indeed, the two shells are not commanded separately but as a whole, through command vectors of 222x1 elements, where the first 111 indices refers to the actuators of the first shell. A command to a single segment is assembled by padding with zeroes the actuators of the other shell.

3.2 Actuators slaving and optical flat

In the M4DP, the actuators lying below the lateral membranes are in charge of compensating the error of the shell vertical position due to the membranes glued on the glass; in the final unit, those actuators will also fall outside the optical pupil, therefore cannot be controlled in close loop. We treated them as *slave* actuators: they apply a static force f_s only, which was calibrated

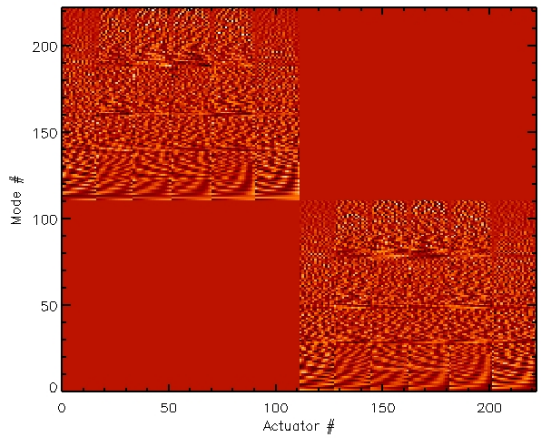

Fig. 2. V matrix assembled as a blocks diagonal matrix: each column represent a mirror mode, with the associated actuator command on the rows.

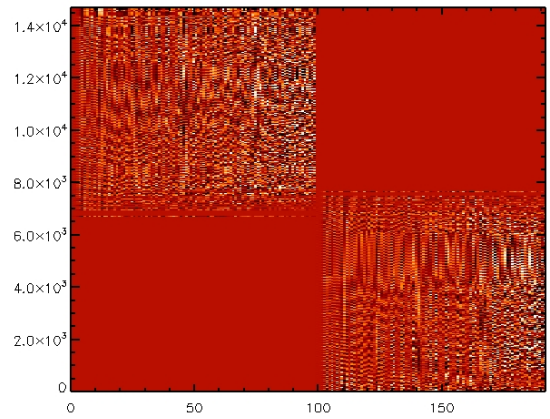

Fig. 3. Optical interaction matrix M of the M4DP: each columns contains the pixel values of a phasemap representing a mirror mode.

to counteract the membranes deformation. For any differential command, the resulting differential force on the slave actuators is always zero.
The *slaving* procedure consists in manipulating the FF matrix; here we recall that after indexing FF according to master-slave order, the actuator force may be written as[8]:

$$\begin{pmatrix} f_a \\ f_s \end{pmatrix} = \begin{pmatrix} FF_{aa} & FF_{as} \\ FF_{sa} & FF_{ss} \end{pmatrix} \begin{pmatrix} p_a \\ p_s \end{pmatrix} \tag{1}$$

where p is the wanted displacement and the subscripts a and s refer to *master* and *slave* actuators, respectively. Putting $f_s = 0$, eq.1 may be solved for the p_s obtaining

$$p_s = S\, p_a = -FF_{as} FF_{ss}^{-1} FF_{sa} p_a; \tag{2}$$

$$FF_r = \begin{pmatrix} FF' & 0 \\ 0 & 0 \end{pmatrix} = \begin{pmatrix} FF_{aa} - S & 0 \\ 0 & 0 \end{pmatrix} \tag{3}$$

At last, a new command matrix V_r may be assembled in the form

$$V_r = \begin{pmatrix} V' & 0 \\ S\,V' & 0 \end{pmatrix} \tag{4}$$

where V' is computed from singular value decomposition of FF'.
The slaving affects the performances of the flattening procedure. The flattening consists in the minimization of the WFE over a given area where both the IF and the current phasemap are defined. The slaving reduces the number of degrees of freedom of the system; it follows that the correction of an area including slave actuators yields a poorer result with respect to flattening an area with all the actuators active, because of the lower density of controlled modes; on the opposite, it is possible to achieve better performances by means of reducing the optical area and masking out the slave actuators. Both strategies are viable and are chosen according to the use cases: in Sec.4.3 we will discuss the flattening performances in some relevant configurations.

3.3 Interaction matrix: sampling and manipulation

The interaction matrix M is the collection of the phasemaps of the system stiffness modes, i.e. the command vectors in V_r. We recall here that each command in V_r is defined on a single shell only, as from Sec.1, so that we could consider, for each mode in V_r, an active-shell S_a and a not-active shell S_u; accordingly, each phasemap W_i is composed by two islands, W_a and W_u associated with S_a and S_u, respectively.
The *slaving* procedure to compute the V_r reduced the degrees of freedom of the system; consequently, the pixel corresponding to the *slave* actuators were rejected for the collection of the interaction matrix. M was built up according to the following procedure:

1. the phasemap W_i of the mode V_{r_i} was sampled with a $push-pull$ technique; the i-th command amplitude was tuned to maximize the SNR and avoid fringes density saturation;
2. the tip-tilt plane is measured on W_u and subtracted from W_a, to get rid of the vibration noise and retrieve the optical tip-tilt associated with the command V_{r_i};
3. $W_u = 0$; $< W_a > = 0$;
4. W_i is stored as the M_i column; the procedure is iterated for all the modes.

The M matrix obtained is an interlaced block matrix (see Fig.3), where the actuators of a single shell produce a deformation on the corresponding island only.
The control matrix R is obtained with pseudo-inversion of M; 2 singular vectors have been discarded, as the piston signal on S_a and S_u was eliminated from the dataset. The singular values spectrum and the discarded eigenmodes are shown in Fig. 4.

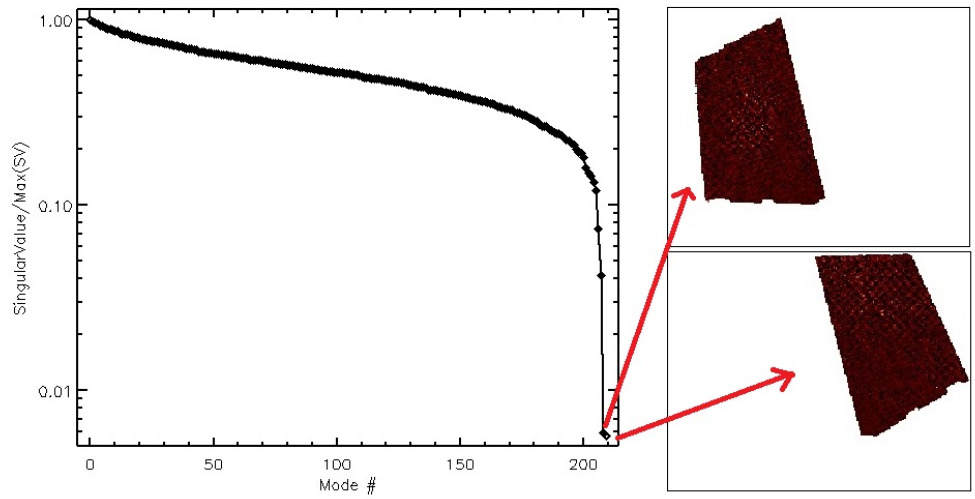

Fig. 4. Spectrum of the singular values of the optical interaction matrix and the discarded eigenmodes.

3.4 High orders and local tip-tilt correction

The flattening procedure consists in the computation of the actuator command

$$f_a = -RW_c = -M^{-1}W_c$$

which corrects the current wavefront W_c with the modes in M. Because of the blocks structure of V_r and M, the procedure will be simultaneously effective on both shells for high orders and alignment aberrations, producing $zero - fringes$ images. Such over-correction comes from the definition of M; in order to correct separately local shapes and global ones (like the alignment), the wavefront W_c was manipulated as follows:

1. W_c is divided into two islands W_1 and W_2 corresponding to the two shells;
2. tilt, focus and coma coefficients Z_{i1} and Z_{i2} have been measured separately on W_1 and W_2;
3. each Zernike shape has been defined over the entire M4DP area and scaled with the corresponding average coefficient;
4. W_c was then corrected with the average aberration.

W_c contains now *local* aberrations only and the flattening procedure may be run without yielding any over-correction. The global tilt will be corrected by aligning the optics.

3.5 Calibration of the internal metrology

The M4DP system, as well as the final unit, is equipped with an internal metrology based on co-located capacitive sensors. The calibration is based on the measurements of a sequence of differential shapes spanning the actuators command range, comparing in the end the optical position with the electrical reading. In order to reconnect correctly the frames in space, some actuators are kept at zero displacement at each step and are therefore considered as markers. The procedure calibrates the gain of the internal metrology only; its offset was adjusted with the optical flattening. More details may be found in [9], where the case of the LBT-ASM is discussed.
For the M4DP we adopted the following strategy:

- the calibration procedure was run separately for each shell;
- the optical alignment was optimized for the active shell in order to have an almost uniform command for all the actuators (i.e. no actuator correction of the differential tilt);
- the not active shell was kept flat during the calibration run in order to have a good fringes visibility;
- both active and not active shell were measured simultaneously; the signal on the not active shell was analysed to check the measurement noise.

3.6 Zernike fitting error test

The Zernike fitting error test consists in the application of 10 μm WF open loop Zernike command (the first 10 modes only are requested, computed over the M4 optical area) and in the measurement of the resulting fitting error. Applied to the M4DP, such command is composed by a large pure piston offset plus a higher order deformation on both shells.
We considered a test procedure based on the flattening of a WF offset, as follows:

1. a circular area (corresponding to the M4 pupil) is considered and the first 10 Zernike modes Z_i are computed over such area;
2. the modal shape Z_i is cropped according to the M4DP foot-print on the final unit (here, both shells are considered), obtaining the shape $Z_{i_{DP}}$;
3. the mean value $P_{Z_i} =< Z_{i_{DP}} >$ is computed

4. $Z_{i_{DP}}$ is transformed according to RCT geometry, then is masked with the current M4DP interferometer mask; a new shape $Z_{i_{DP'}}$ is obtained, corresponding to the expected WF signal of the Z_i as seen on the M4DP in RCT configuration;
5. an open loop piston command P_{Z_i} is sent and the resulting phasemap $s_{Zp_i}$is measured, where the subscript p is for piston only;
6. the flattening computation is run on the $s_{Zp_i} + Z_{i_{DP'}}$ shape, producing a final phasemap s_{Z_i};
7. the difference $s_{Z_i} - Z_{i_{DP'}}$ is the fitting error of the $i - th$ Zernike mode.

In Fig.5 some Z_i shapes are shown with the location of the M4DP actuators on the M4.

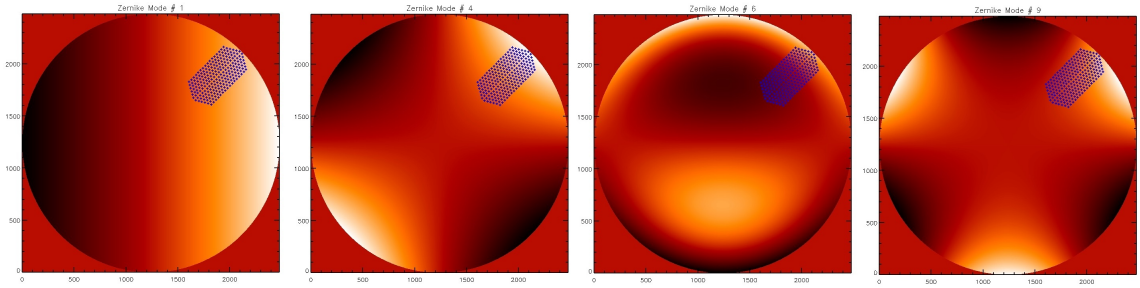

Fig. 5. Zernike shapes cropped according to the DP geometry on M4.

4 Optical test results

The optical testing was carried out at INAF-Merate Observatory in Italy through february and march 2015. In the following we will report the most relevant results of the laboratory activity.

4.1 Flattening results

A preliminary flattening on both shell was obtained by applying the first 10 mirror modes with random amplitude, in order to reduce the local fringes density and enlarge consequently the visible area. As soon as the full mirror was within the interferometer capture range, the flattening procedure as in Sec.3.4 was run simultaneously on both shells. In Fig.6 the fringes pattern corresponding to the different steps of the flattening procedures are shown. The final figuring error, after removing global tilt (the local-differential tilt was corrected with the flattening) is 12 nm RMS WFE. The area corresponding to the membranes showed a residual deformation at the inter-actuator scale, as a result of the stress release after flattening that area: it was therefore not considered in the WFE computation. A typical flattening realization is shown in Fig.7. The correction of the differential piston was not in the scope of the optical test and it was not considered as a part of the flattening procedure nor of the performace verification: we simply aligned the interference fringes on both shell, measuring a final differential mean WF of 8 nm.

4.2 Zernike test

The test was run according to the procedure in Sec.3.6: we considered two test realizations, with modal amplitude of 10 μm and 5 μm PtV. Each test sequence took approximately 90 minutes to

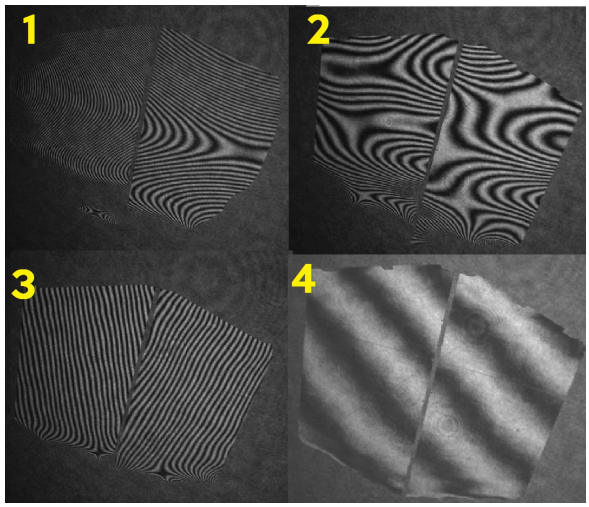

Fig. 6. Interferometer images of the flattening procedure. 1): system aligned on the DP; 2): low order modes corrected to improve the fringes visibility; 3): high orders corrected separately on both shells; 4): shells co-phased after simultaneous correction of high orders, local tip/tilt and differential piston.

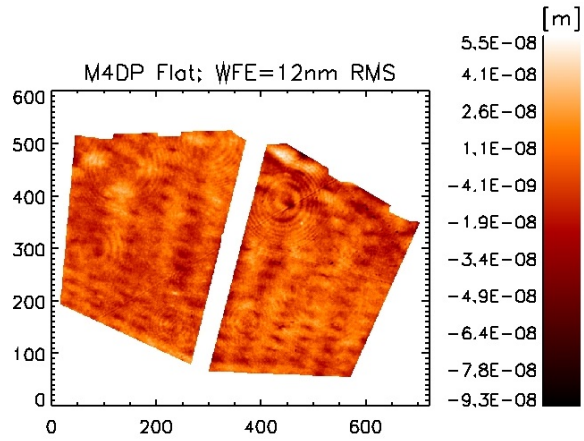

Fig. 7. Flattening result on the M4DP. The WFE after subtraction of the global tip/tilt is 12 nm RMS.

collect the 10 Zernike shapes, trying to improve the accuracy by time averaging the convection noise. On the second hand, we expected a larger tip/tilt drift during a longer time integration; tip/tilt cannot be removed from the result phasemaps as we want to measure the accuracy of the full command, tip/tilt included.
During the data analysis we compared the resulting phasemaps s_{Z_i} with the simulated ones $Z_{i_{DP'}}$ to compute the fitting error. The results for the 10 μm case is shown in Fig.8, together with the specification value for the M4 case. The tip/tilt noise is also presented to show its contribution in the residual. The measured fitting error is in the range 30 nm ÷ 40 nm RMS WF, including 5 nm ÷ 35 nm RMS WF from tilt residual. The value is then comparable with the final flattening, where we removed the phasemap global tilt. The matching was expected, the Zernike test consists indeed in flattening the mirror with a given WF offset. Differently from the flattening case, as we mentioned, the residual tip/tilt cannot be removed here as it was in the WF offset. It would be possible to improve the measurement accuracy by averaging many test realizations in order to reduce the tilt noise.

4.3 Optical result of the slaving procedure

We measured the WFE degradation due to the actuator slaving. We recall here that the actuators below the lateral membranes were slaved to avoid forces saturation: they shall provide the static force to compensate for the membranes deformation only.

As an initial reference, we measured the flattening result over the entire optical area with all the actuators active. The result is shown in panel *a* of Fig.10. We then considered two configurations: with 1 row of slave actuators and with 3 rows, per shell. For each configuration, we adjusted the interferometer mask in order to include or reject the area corresponding to the slave actuators; for all the cases, we measured the WFE value over the entire optical area, over

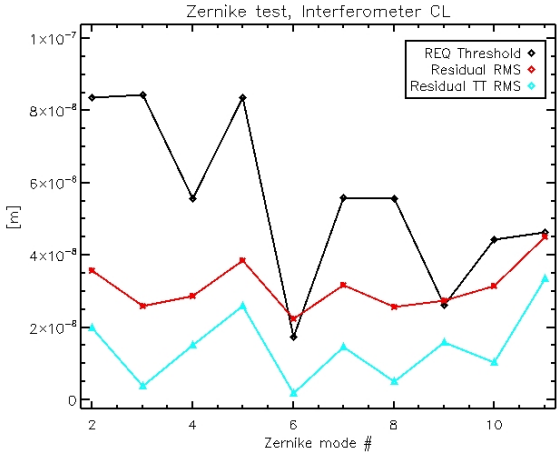

Fig. 8. Result of the Zernike test. Red plot: WFE difference between the analytical shape and the actual result on the M4DP; blue plot: tip/tilt residual throughout the test procedure; black plot: difference threshold from specification.

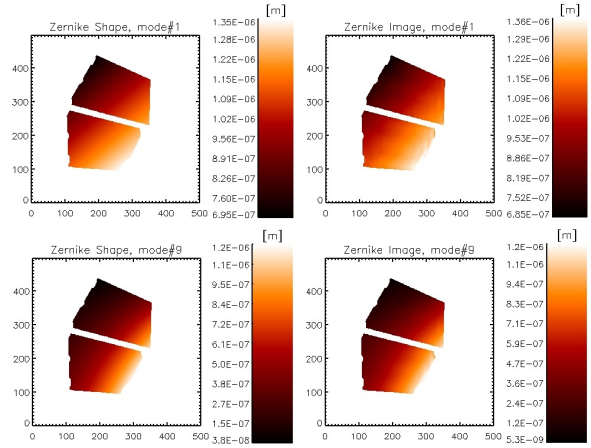

Fig. 9. Result of the Zernike test for modes 1 and 9: comparison between analytical shape (left) and actual result on the M4DP.

the optical area without the membranes and on a sub-frame 4 rows away from the slave area. The results are shown in Tab.1; in Fig.10 we present the corresponding phasemaps. As a comparison, the final flattening result (12 nm RMS WF) was optimized by slaving 3 actuator rows, reducing the controlled area until the 4th row and rejecting it from the computation of the WFE: the same value is obtained with all the actuators and excluding the membranes area from the computation of the WFE (corresponding to configuration *a*).

The results in Tab. 1 may be summarized as follows:

- the WFE measured on the subframe is similar for all the cases, indicating that the procedure doesn't degrade the performance far from the slaved area; it is also comparable to the final flattening result after optimizing the slaved area;
- the case of slave actuators and full optical area (configuration *b*) yields the poorest result in terms of WFE, because of the lower density of degrees of freedom;
- after slaving, the flattening result over a controlled area (i.e. after masking the slave area) is similar to the case of all actuators active (cases *c* and *d* versus *a*); the slightly larger WFE is due to the residual interactuator deformation due to stress release as explained before;
- the results in *c* and *d* might be improved by adjusting the static command on the slave actuators to minimize the stress release over the controlled area; such solution will be however valid for the flat case only, with the current configuration of local/global tilt.

4.4 Analysis of the differential piston signal

We investigated the accuracy and the precision of the measurement of the differential piston $\Delta\pi$. A few points need to be addressed here. First, the piston signal measured by interferometer suffers from phase ambiguity (i.e. the interferometer SW identifies the islands in the phasemap and assign to each of them a random quantized phase $\theta = \lambda/2$); second, the air convection is responsible for a spurious non zero-mean value noise on each shell; third, the $\Delta\pi$ measurement

Act. configuration	Optical area	WFE on optical area nm RMS	WFE w/o membranes nm RMS	WFE on subframe nm RMS
a: No slave acts.	Full	23	12	13
b: 1 row slave acts.	Full	72	21	13
c: 1 row slave acts.	-1 row	28	16	14
d: 3 row slave acts.	-3 rows	24	17	13

Table 1.

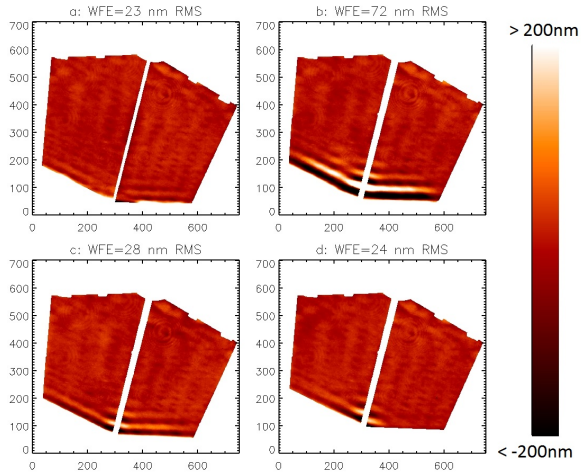

Fig. 10. Phasemaps corresponding to the 4 test configurations as in Tab.1.

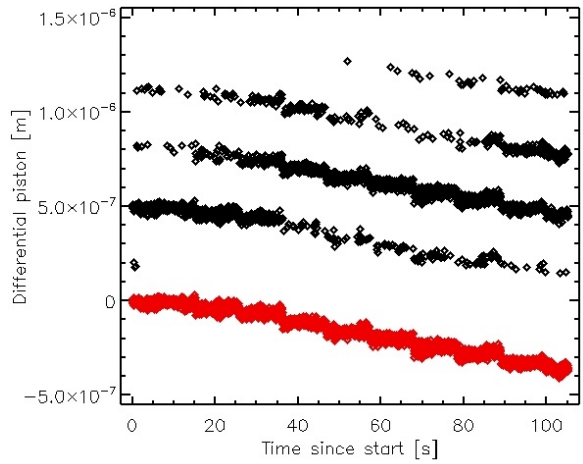

Fig. 11. Test result of the levelling algorithm: one shell was moved with respect to the other with 50 nm piston commands. Black plot: raw data; red plot: result of the levelling algorithm.

accuracy should be cross-checked with a reference monolithic mirror split into two islands, where $\Delta\pi$ is zero by definition. The three points were addressed with a sequence of dedicated tests, reported below.

We addressed the phase ambiguity issue by means of a levelling algorithm which adds an arbitrary $n\theta$ offset to reconnect the dataset. An external condition is requested: for instance, for time series measurement we assumed that, frame by frame, the *real* piston variations are lower than $\pm\theta/2$=75 nm; such condition is satisfied under laboratory conditions and the result of the levelling algorithm is shown in Fig.11, where we measured the differential piston between the two shells when applying 40 nm piston commands to one of them.
For the case of IF data we assumed that the piston command associated with each mode is lower than θ. We realized the IF sampling procedure needs to be modified in order to satisfy such condition. In facts, the piston mode is significantly contributed by the first 3 modes only; in order to satisfy the condition for a $push-pull$ measurement, the command amplitude should be lower than $\approx$ 30 nm, which is not optimal for low order modes to guarantee a good SNR. A revised IF sampling strategy is to build up a new mirror modes basis by separating the pure piston from low order modes, then collecting them with large amplitude and eventually to measure the pure piston with low amplitude. Such procedure was not tested during the M4DP activity.

We evaluated the measurement precision and accuracy for a number of experimental configurations, for instance with different thermal gradients within the optical path and with/without bench ventilation or insulation; for each case, we considered a set of 3000 phasemaps, collected at the interferometer frame rate, then we measured the differential piston between the two shells and computed the standard deviation and the mean of the sample. The results is shown in Fig.12, representing the following configurations: M4DP cooler and warmer than ambient temperature, bench ventilation on and off.
The absolute $\Delta\pi$ measurement accuracy was estimated with a monolithic flat mirror, divided into two islands by mean of a suitable mask. The test result is shown in Fig.13. We estimated a measurement accuracy of 2 nm (red plot).

The results of the differential piston tests may be summarized as follows:

- the levelling algorithm is an effective tool to solve the interferometer phase ambiguity issue, provided some conditions on the expected $\Delta\pi$ are satisfied;
- assuming that both shells were stable during the tests, different environment conditions may lead to different accuracy errors in the estimation of the $\Delta\pi$, as it may be observed in Fig.12 and in Fig.13; the same applies for the measurement precision, i.e. the standard deviation of the sample;
- the best accuracy (i.e. $\Delta\pi$=0 with the monolithic mirror) was obtained with the optical bench exposed to laboratory ventilation; this is an expected result, as laboratory ventilation is far more effective than single fans to mix up the air and prevent the formation of quasi static patterns;

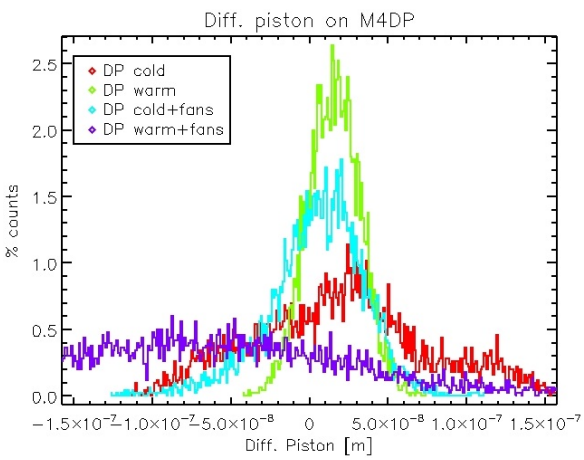

Fig. 12. Distribution of differential piston values measured on the M4DP.

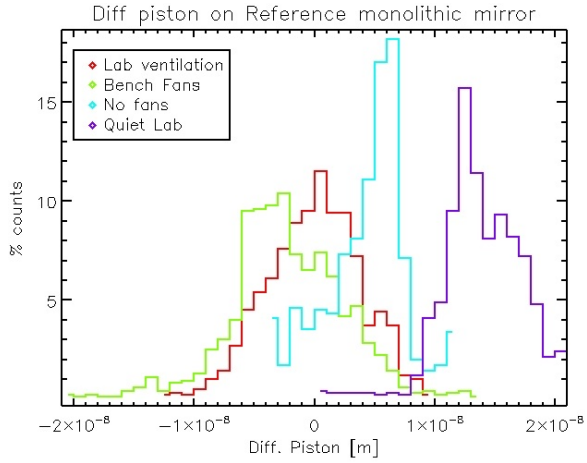

Fig. 13. Distribution of differential piston values measured on reference monolithic flat mirror, divided into two islands with a mask.

5 Conclusion: getting ready for the M4

The test on the M4DP was a valuable experience to get ready for the optical calibration of the M4. A number of key features of the final unit have been taken into account and addressed: the configuration handling and optical control of a segmented deformable mirror; the measurement

and processing of global shapes, i.e. defined over both shells like tip/tilt and power; the differential piston measurement and correction; the computation of global commands to achieve a given WF (e.g. a Zernike shape). The M4 optical test procedure has been in the end consolidated.
Within the M4 project the M4DP system is scheduled to serve as a test bench for a second session of optical activities; these will include also a scaled replica of the M4 optical tower, useful to address the alignment procedures and the evaluation of the measurement accuracy. The optical calibration of the final unit is scheduled to start at the end of 2021.

References

1. Brusa, G., Riccardi, A., Wildi, F. P. et al., Proceedings of the SPIE, *5169*, (2003)
2. Vernet, E., Cayrel, M., Hubin, N. et al., Proceedings of the SPIE, *9148*, (2014)
3. Riccardi, A., Xompero, M., Briguglio, R. et al., Proceedings of the SPIE, *7736*, (2010)
4. Briguglio, R., Xompero, M., Riccardi, A. et al., Proceedings of the Third AO4ELT Conference, (2013)
5. Molinari, E., Tresoldi, D., Toso, G., Spano', P., Mazzoleni, R., Riva, M., Riccardi, A., Biasi, R., Andrighettoni, M., Angherer, G., Gallieni, D., Tintori, M., Marque, G., Proceedings of the SPIE, *7736*, (2010)
6. Shu, K. L., Applied Optics *22*, (1983)
7. Riccardi, A., Brusa, G., Del Vecchio, C., et al., European Southern Observatory Conference and Workshop Proceedings, *58*, (2002)
8. Riccardi, A., Arcetri Technical Reports, http://www.arcetri.astro.it/ricerca/rapporti-tecnici/205-reports/584-12-1, *1*, (2012)
9. Briguglio, R., Xompero, M., Riccardi, A., Biasi, R., Andrighettoni, M., Proceedings of the SPIE, *8447*, (2012)
10. Vernet, E., Cayrel, M., Hubin, N., Biasi, R., Gallieni, D., Tintori, M., Proceedings of the SPIE, *9148*, (2014)
11. Pariani, G., Briguglio, R., Xompero, M., Riccardi, A., Riva, M. et al., Proceedings of the SPIE, *9145*, (2014)